

Realistically Coupled Neural Mass Models Can Generate EEG Rhythms

Roberto C. Sotero

rcarlos@cneuro.edu.cu

Nelson J. Trujillo-Barreto

trujillo@cneuro.edu.cu

Yasser Iturria-Medina

iturria@cneuro.edu.cu

Cuban Neuroscience Center, Brain Dynamics Department, Havana, Cuba

Felix Carbonell

felix@icmf.inf.cu

Juan C. Jimenez

jcarlos@icmf.inf.cu

Instituto de Cibernética Matemática y Física, Departamento de Sistemas Adaptativos, Havana, Cuba

We study the generation of EEG rhythms by means of realistically coupled neural mass models. Previous neural mass models were used to model cortical voxels and the thalamus. Interactions between voxels of the same and other cortical areas and with the thalamus were taken into account. Voxels within the same cortical area were coupled (short-range connections) with both excitatory and inhibitory connections, while coupling between areas (long-range connections) was considered to be excitatory only. Short-range connection strengths were modeled by using a connectivity function depending on the distance between voxels. Coupling strength parameters between areas were defined from empirical anatomical data employing the information obtained from probabilistic paths, which were tracked by water diffusion imaging techniques and used to quantify white matter tracts in the brain. Each cortical voxel was then described by a set of 16 random differential equations, while the thalamus was described by a set of 12 random differential equations. Thus, for analyzing the neuronal dynamics emerging from the interaction of several areas, a large system of differential equations needs to be solved. The sparseness of the estimated anatomical connectivity matrix reduces the number of connection parameters substantially, making the solution of this system faster. Simulations of human brain rhythms were carried out in order to test the model. Physiologically plausible results were obtained based on this anatomically constrained neural mass model.

1 Introduction

We aim at describing a generative model of EEG rhythms based on anatomically constrained coupling of neural mass models. Although the biophysical mechanisms underlying oscillatory activity in neurons are well studied, the origin and function of global characteristics (such as EEG rhythms) of large populations of neurons are still unknown. In this context, computational models have proven capable of providing insight into this problem. Two modeling approaches have been used to study the behavior of neuronal populations. One approach is based on the study of large computational neuronal networks in which each cell is realistically represented by multiple compartments for the soma, axon, and dendrites, and each synaptic connection is modeled explicitly (Traub & Miles, 1991). A disadvantage of such realistic modeling is that it requires high computational power. For this reason, simplified versions of such models in which only one compartment model was taken into account have been used (Wang, Golomb, & Rinzel, 1995; Rinzel, Terman, Wang, & Ermentrout, 1998). However, even in this case, the use of such detailed models makes it difficult to determine the influence of each model parameter on the generated average network characteristics. The second approach is based on the use of neural mass models (NMM). In contrast to neuronal networks, NMMs describe the dynamics of cortical columns and brain areas by using only a few parameters, but without much detail. In this approach, spatially averaged magnitudes are assumed to characterize the collective behavior of populations of neurons of a given type instead of modeling single cells and their interactions in a detailed network (Wilson & Cowan, 1972; Lopes da Silva, Hoeks, Smits, & Zetterberg, 1974; Zetterberg, Kristiansson, & Mossberg, 1978; van Rotterdam, Lopes da Silva, van den Ende, Viergever, & Hermans, 1982; Jansen & Rit, 1995; Valdes, Jiménez, Riera, Biscay, & Ozaki, 1999; Wendling, Bellanger, Bartolomei, & Chauvel, 2000; David & Friston, 2003).

Despite their simplicity, NMMs have been very helpful in the study of EEG rhythms. For example, in order to study the origin of the alpha rhythm, Lopes da Silva et al. (1974) developed an NMM comprising two interacting populations of neurons, the thalamocortical relay cells and the inhibitory interneurons, which were interconnected by a negative feedback loop. Later, this model was extended to include both positive and negative feedback loops (Zetterberg et al., 1978; Jansen, Zouridakis, & Brandt, 1993). In Jansen and Rit (1995), alpha and beta activities were replicated by using two coupled neural mass models representing cortical areas with delays in the interconnections between them. Wendling et al. (2000) investigated the generation of epileptic spikes by extending Jansen's model to multiple coupled areas but explored the dynamics of only three areas for different values of the connectivity constants. David and Friston (2003) considered that a cortical area comprises several noninteracting neuronal populations that were in turn described by Jansen's models. This model allowed them

to reproduce the whole spectrum of EEG signals by changing the coupling between two of these areas, thus showing the importance of parameters related to the coupling between different brain regions for the resulting dynamics.

Due to the lack of information about actual connectivity patterns, previous approaches have been devoted to the study of the temporal evolution of neuronal populations rather than their spatial dynamics. However, the development of techniques such as diffusion weighted magnetic resonance imaging (DW MRI) in the past 20 years makes noninvasive study of the anatomical brain circuitry of the living human brain possible. This has put at our disposal extremely valuable information and gives us a unique opportunity to formulate models that take into account a more realistic view of the central nervous system.

In this article, we extend Jansen's model to characterize the dynamics of a cortical voxel. Building on this, our goal is to study the rhythms obtained when coupling several areas comprising large numbers of interconnected voxels. In this approach, voxels of the same cortical area are assumed to be coupled with excitatory and inhibitory connections (short-range connections), while connections between areas (long-range connections) are assumed to be excitatory only. This is an extension of the model of David and Friston (2003) because interactions between voxels within the same area are taken into account. Additionally, we introduce anatomical constraints on coupling strength parameters (CSP) between different brain regions. This is accomplished by using CSPs estimated from human DW MRI data (Iturria-Medina, Canales-Rodríguez, Melié-Garcia, & Valdés-Hernández, 2005). The thalamus is also modeled using a single NMM, mutually coupled with the cortical areas. We show that this anatomically constrained NMM can reproduce the EEG rhythms recorded at the scalp, another step in the validation of NMMs as a valuable tool for describing the activity of large populations of neurons.

The letter is organized as follows. In section 2, the NMMs used for a cortical voxel and the thalamus are formulated. Section 3 is devoted to the modeling of short-range and long-range interactions. The integrated thalamocortical model is formulated in section 4. In section 5 the observation model that links the activity in a cortical voxel with the recorded EEG on the scalp surface is presented. Section 6 describes the numerical method used for integrating the huge system of random differential equations obtained. Finally, sections 7 and 8 are devoted to a description of the simulations as well as a discussion of the results.

2 Models for a Cortical Voxel and the Thalamus

In this work we model the neuronal activity in a cortical voxel by extending previous neural mass models that have been used to describe neural dynamics at smaller spatial scales. In particular, Jansen and Rit (1995)

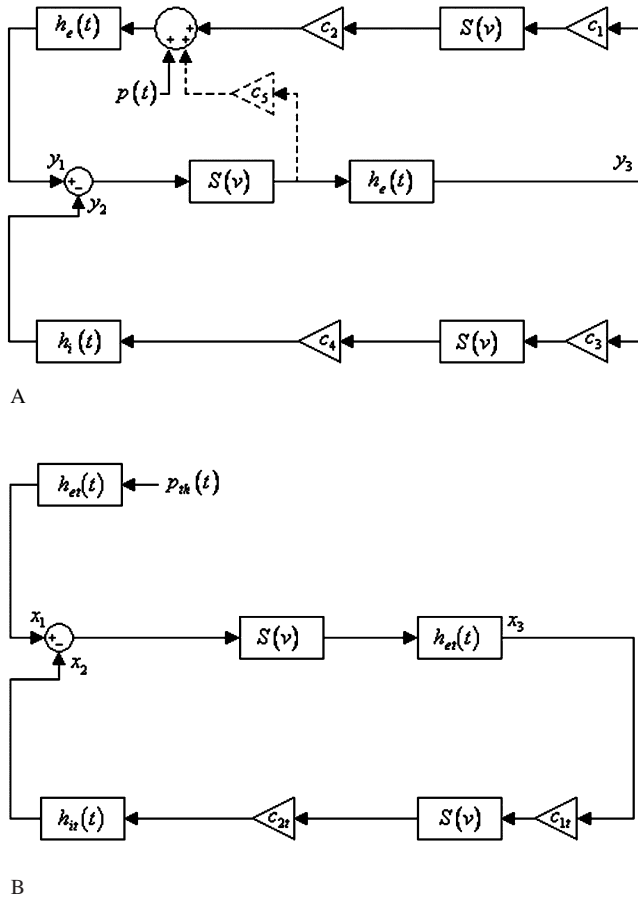


Figure 1: The basic neural mass models used. (A) Model for a cortical voxel. The dynamics is obtained by the interaction of three populations of neurons: excitatory pyramidal cells, excitatory spiny stellate cells, and inhibitory interneurons (smooth stellate cells). Input to the system is modeled by the pulse density $p(t)$. This reduces to Jansen's model when removing the dashed-line loop. (B) Model for the thalamus. Interaction between one excitatory and one inhibitory subpopulation, representing thalamocortical and reticular-thalamic neurons, respectively.

studied the temporal dynamics of a cortical column by means of the interaction of interconnected populations of excitatory pyramidal and stellate cells as well as inhibitory interneurons. This model (see Figure 1A, except for the dashed-line loop) capitalizes on the basic circuitry of the cortical column (Mountcastle, 1978, 1997). Pyramidal cells receive feedback from

excitatory and inhibitory interneurons, which receive only excitatory input from pyramidal cells. Nevertheless, at the spatial scale of voxels, this simplified circuitry is no longer valid, but more complicated interactions need to be considered. While a cortical column has a diameter of 150 to 300 μm , the length of a voxel usually ranges from 1 to 3 mm, comprising several interconnected columns. At this spatial scale, pyramidal-to-pyramidal connections become increasingly important, accounting for the majority of intracortical fibers (Braitenberg & Schüz, 1998). In our approach, Jansen's model is extended to include this kind of connection by adding a self-excitatory loop for the pyramidal population (see Figure 1B). Zetterberg et al. (1978) had already used a generic model of this kind for describing the temporal dynamics of a neuronal mass consisting of two excitatory and one inhibitory population. Although they were able to produce signals resembling EEG background activity, their model had no specific neural substrate.

Usually in this type of modeling, the dynamics of each neuronal population is represented by two transformations (Jansen & Rit, 1995; Zetterberg et al., 1978). First, the average pulse density of action potentials entering a population is converted into an average postsynaptic membrane potential by means of linear convolutions with impulse responses $h_e(t)$ and $h_i(t)$ for the excitatory and the inhibitory case, respectively:

$$h_e(t) = A a t e^{-at} \quad (2.1)$$

$$h_i(t) = B b t e^{-bt}. \quad (2.2)$$

Parameters A and B represent the maximum amplitude of excitatory (EPSP) and inhibitory postsynaptic potentials (IPSP), respectively, while lumped parameters a and b depend on passive membrane time constants and other distributed delays in the dendritic network.

The second (nonlinear) transformation accounts for the conversion of average membrane potentials of the population into an average pulse density of action potentials, which is accomplished by means of a sigmoid function,

$$S(v) = \frac{2e_0}{1 + e^{r(v_0 - v)}}, \quad (2.3)$$

where $2e_0$ is the maximum firing rate, v_0 is the postsynaptic potential (PSP) corresponding to firing rate e_0 , and parameter r controls the steepness of the sigmoid function.

The interaction between the different populations is characterized by five connectivity constants c_1, c_2, c_3, c_4, c_5 (see Figure 1A), which represent the average number of synaptic contacts. The first four constants have the

same interpretation as in Jansen and Rit (1995) and were related in that work based on physiological arguments:

$$c_2 = 0.8c_1, c_3 = c_4 = 0.25c_1. \quad (2.4)$$

Similarly, c_5 accounts for interactions between pyramidal cells. Using Laplace transforms, this convolution model can easily be expressed in terms of the following system of differential equations:

$$\begin{aligned} \dot{y}_1(t) &= y_4(t) \\ \dot{y}_2(t) &= y_5(t) \\ \dot{y}_3(t) &= y_6(t) \\ \dot{y}_4(t) &= Aa \{ p(t) + c_5 S(y_1(t) - y_2(t)) + c_2 S(c_1 y_3(t)) \} - 2ay_4(t) - a^2 y_1(t) \\ \dot{y}_5(t) &= Bbc_4 S(c_3 y_3(t)) - 2by_5(t) - b^2 y_2(t) \\ \dot{y}_6(t) &= Aa S(y_1(t) - y_2(t)) - 2ay_6(t) - a^2 y_2(t), \end{aligned} \quad (2.5)$$

where $y_1(t)$, $y_3(t)$ are average EPSP and $y_2(t)$ is the average IPSP (see Figure 1A).

From classical electrophysiology, pyramidal cells are considered to be the main contributors to the measured EEG at the scalp surface. This is also known to stem from two basic reasons: (1) the specific location of excitatory and inhibitory synaptic inputs on the pyramidal neuron and (2) the spatial organization of these cells in the form of a palisade oriented perpendicular to the cortex (Niedermeyer & Lopes da Silva, 1987; Nunez, 1981). That is, afferent excitatory connections make contact predominantly on apical dendrites, creating an extracellular negative potential (sink of current due to Na^+ entering the cell), while inhibitory synapses reach mainly the soma of the neuron, creating an extracellular positive potential (source of current due to Cl^- entering the cell). Thus, at a macroscopic level, the potential field generated by a synchronously activated palisade of neurons behaves like that of a dipole layer and can be considered the basis of EEG generation. Note that in our approach, $y_1(t)$ and $y_2(t)$ are the result of excitatory and inhibitory synapses acting on the pyramidal cell population. Thus, the difference $y_1(t) - y_2(t)$ can be taken in a fairly good approximation to be proportional to the EEG signal (Jansen & Rit, 1995).

The input to the model in Figure 1A is the process $p(t)$, which represents the basal stochastic activity within the voxel plus the extrinsic input. This extrinsic input does not include afferences from voxels of the same and other cortical areas, but it models specific stimulus-dependent input that modulates the activity of the neuronal population.

Additionally, our approach capitalizes on specific properties of the thalamic nuclei in order to model the contribution of this subcortical structure,

which is the main relay station of the sensory input on its way to the cortex. That is, the thalamus comprises two major populations of neurons: thalamocortical (TC) excitatory relay neurons and thalamic inhibitory reticular (RE) neurons. Only the axons of TC neurons project to the cortex, while RE neurons form an inhibitory network that surrounds the thalamus and project inhibitory connections to TC neurons exclusively (Destexhe & Sejnowski, 2001). This circuitry allowed us to formulate the mass model shown in Figure 1B, which Lopes da Silva et al. (1974) used for simulating the alpha rhythm. Note that the model is used to describe the dynamics of the thalamus as a whole, without taking into account any subdivision into voxels. The motivation for this was the physical separation of the two types of neuronal populations that form the thalamus. On the other hand, the absence of any preferential orientation of the neurons in the thalamus, together with the depth of this structure, has led to the idea that it does not generate any measurable voltage at the scalp surface. Thus, in our approach, no direct thalamic contribution to the EEG is considered. A more sophisticated model of the thalamic activity could be used to elucidate its actual contribution to the EEG generation, but that would entail a detailed knowledge of its microscopic cytoarchitectonic organization, which we lack at the moment.

3 Short-Range versus Long-Range Interactions

If we want to model the dynamics of macroscopic cortical areas, we have to augment the model described to account for the specific neuronal interactions in the brain. In the cytoarchitectonic organization of the cerebral cortex, two types of connections can be distinguished: short-range and long-range connections (SRC and LRC, respectively). SRCs are made by cortical neurons with local branches that can reach a maximum of about 10 mm (Braitenberg, 1978; Abeles, 1991; Jirsa & Haken, 1997) corresponding to the length of the longest horizontal axon collaterals plus the length of the longest dendrites. LRCs are mainly formed by axons of pyramidal cells that cross the white matter and connect cortical regions that can be up to 100 mm apart (Abeles, 1991; Jirsa & Haken, 1997).

Several differences between these two systems can be established, not only in their characteristic lengths but also in their specificity and function (Abeles, 1991; Braitenberg & Schüz, 1998). While SRCs can be described in statistical terms, with an effective connection strength that diminishes exponentially with the distance between neuronal populations, LRCs do not show such a regular and smooth pattern but have a high degree of specificity. Additionally, LRCs terminate preferentially on the apical dendrites of pyramidal cells, while local collaterals terminate more on basal dendrites. In the following sections, we describe how this differentiation of cortical interactions is incorporated into our model.

3.1 Within-Area Interactions. First, SRCs that mediate neuronal interactions within a cortical area will be described. A diagram of the proposed augmented model for a given voxel is shown in Figure 2A. We assume that voxels of the same area are coupled by means of both excitatory and inhibitory connections, where the pyramidal cell population is the target of all the input to the system. Excitatory input comes from pyramidal and spiny stellate cell populations with coupling strengths described by connectivity functions that depend on the distance between voxels $|x_m - x_j|$ (Jirsa & Haken, 1996, 1997):

$$k_{e1}^{mj} = \frac{1}{2\sigma_{e1}} e^{-\frac{|x_m - x_j|}{\sigma_{e1}}} \quad (3.1)$$

$$k_{e2}^{mj} = \frac{1}{2\sigma_{e2}} e^{-\frac{|x_m - x_j|}{\sigma_{e2}}}. \quad (3.2)$$

In equations 3.1 and 3.2, k_{e1}^{mj} and k_{e2}^{mj} are the strengths of the connections that pyramidal cells and excitatory interneurons of voxel m make on pyramidal cells of voxel j , respectively. Delays in these connections can be modeled by linear transformations similar to equation 2.1, as in Jansen and Rit (1995). We use $h_{d2}(t)$ and $h_{d3}(t)$, respectively:

$$h_{d2}(t) = Aa_{d2}te^{-a_{d2}t} \quad (3.3)$$

$$h_{d3}(t) = Aa_{d3}te^{-a_{d3}t}. \quad (3.4)$$

Similar equations are formulated for within-area inhibitory connections, which are considered by means of the connection strength k_i^{mj} that inhibitory interneurons (smooth stellate cells) of voxel m exert on pyramidal cells of voxel j , that is,

$$k_i^{mj} = \frac{1}{2\sigma_i} e^{-\frac{|x_m - x_j|}{\sigma_i}} \quad (3.5)$$

$$h_{d4}(t) = Bb_{d4}te^{-b_{d4}t}. \quad (3.6)$$

3.2 Between-Area Interactions. Interactions between distant cortical areas are determined by LRCs, which in our approach are mediated by pyramidal-to-pyramidal cell connections. There is no clarity about the rules governing the system of LRCs (Braitenberg & Schüz, 1998). Nevertheless, the emergence of new imaging techniques like diffusion weighted magnetic resonance imaging (DW MRI) in the past few years has opened a window to the study of this type of connection in the living human brain. DW MRI is based on the fact that trajectories followed by water molecules during diffusion processes reflect the microscopic environment of brain tissues. Then nervous fibers can be characterized by tracing probabilistic paths

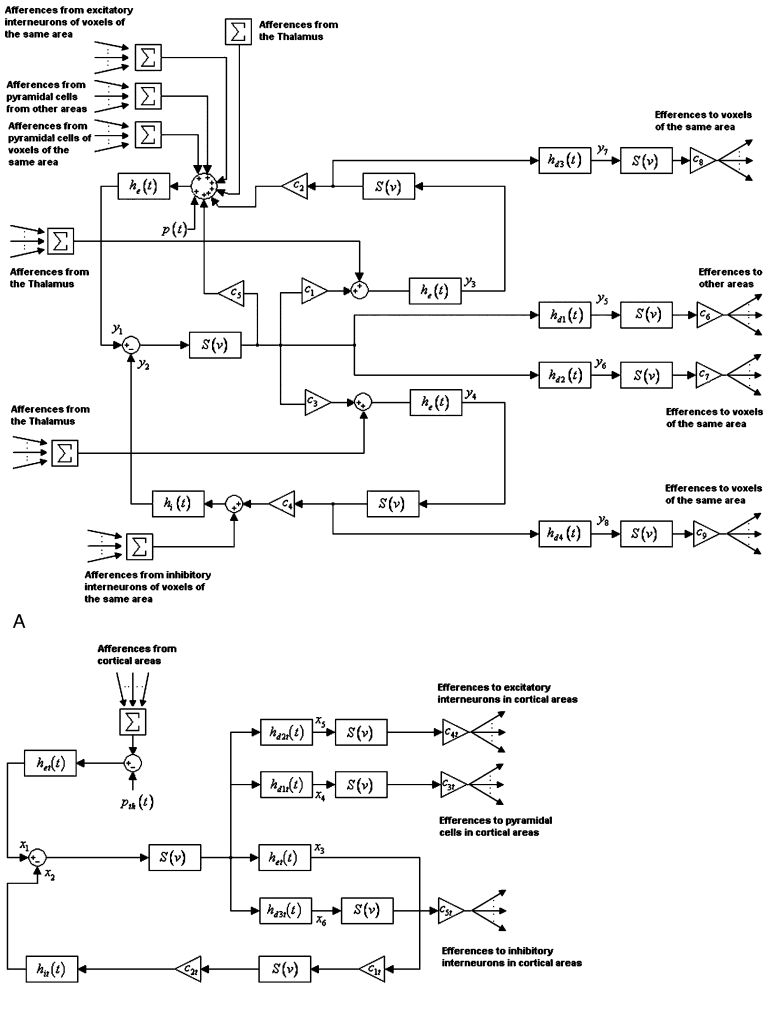


Figure 2: The thalamocortical model. (A) Input-output relationship for the neural mass model of a cortical voxel. A cortical voxel receives excitatory afferences from pyramidal cells and excitatory stellate cells of voxels of the same area, from pyramidal cells of other cortical areas, and from TC relay neurons. Inhibitory afferences are received from inhibitory interneurons of voxels of the same area. The pulse density $p(t)$ accounts for the basal stochastic activity within the voxel. (B) Input-output relationship for the neural mass model of the thalamus. TC relay neurons send axonal projections to the cortex, where they make synapses on the three populations of neurons considered. TC cells receive backward connections from cortical pyramidal neurons. The pulse density $p_{th}(t)$ accounts for the background stochastic activity within the thalamus plus stimulus related inputs.

that represent the preferred direction of water diffusion along the nervous fibers in each voxel. Finally, measures of anatomical connectivity reflecting the interrelation between voxels and areas can be defined and calculated based on these paths. In this article, the LRC strength $K^{i,n}$ between two areas i and n will be estimated from actual DWMRI data.

Most work in the field of DWMRI has defined measures of between-voxel rather than between-areas anatomical connectivity. For example, for characterizing the probability of connection of a point R with a point P , one can use the number of probabilistic paths leaving P and entering R divided by the number of probabilistic paths generated in P (Behrens et al., 2003; Hagmann et al., 2003; Parker, Wheeler-Kingshott, & Barker, 2002; Koch, Norris, & Hund-Georgiadis, 2002). In Tuch (2002) the probability of connection between two points is estimated as the probability of the most probable paths joining both points, while in Parker et al. (2002) and Tournier, Calamante, Gadian, & Connelly, (2003), it is taken as the probability of the path that minimizes a cost function depending on diffusion data. However, diffusion data generally show high isotropy within the gray matter, giving poor information about the distribution of nerve fibers. Consequently, in most cases, it is not convenient to trace probabilistic paths within gray matter areas. Another approach for studying connectivity in the brain is to use only the points at the boundaries of gray matter regions for characterizing connection strengths between zones and not between the individual voxels comprising them. In this line of work, Iturria-Medina, Canales-Rodríguez et al. (2005) and Iturria-Medina, Valdés-Hernández et al. (2005) proposed a model for obtaining anatomical connection strengths (ACS) between brain zones. In their method, the ACS between two regions, A and B ($C_{A \leftrightarrow B}$), was defined as being proportional to the cross-section area of the total cylindrical-shaped volume of the nervous fibers shared by these regions. ACS was then calculated as the area occupied by the connector volume over the surfaces of the connected zones,

$$C_{A \leftrightarrow B} = A_{T(A,B)} + B_{T(A,B)}, \quad (3.7)$$

where $A_{T(A,B)}$ and $B_{T(A,B)}$ represent the area defined by fibers (both afferent and efferent), joining A with B over the surface of A and B , respectively. These areas were evaluated from a DWMRI data set by measuring the number of target voxels on each surface of the generated probabilistic paths that simulate fiber trajectories under the assumption that those paths are contained inside the connector volume.

Notice that methods for reconstructing fiber paths using DWMRI data cannot distinguish between excitatory and inhibitory connections. However, in the proposed model, LRCs are considered to be excitatory only. This assumption is consistent with physiological and anatomical studies, demonstrating, that pyramidal cells of layer III are the main source of the

feedforward projections to other cortical areas (Gilbert & Wiesel, 1979, 1983; Martin & Whitteridge, 1984; McGuire, Gilbert, Rivlin, & Wiesel, 1991; Douglas & Martin, 2004). Thus, information obtained from DWMRI data can be used as a measure of the CSP ($K^{i,n}$) between any two given areas i and n .

For modeling delays in long-range connections, we use

$$h_{d1}(t) = Aa_{d1}te^{-a_{d1}t}. \quad (3.8)$$

Like parameters a and b of Jansen's model, constants a_{d1}, a_{d2}, a_{d3} , and b_{d4} account for passive membrane time constants and other distributed delays in the dendritic network.

4 Thalamocortical Model

In this section we present the final mathematical formulation of the thalamocortical model proposed, with SRCs and LRCs included.

As shown in Figure 2A, intra- and intervoxel interactions are described by nine connectivity constants, from c_1 to c_9 . The first five constants, c_1 to c_5 , have already been defined in section 2. Constant c_6 represents the number of synapses made by pyramidal cells of one voxel on voxels of other areas, c_7 is the number of synapses made by pyramidal cells on voxels of the same area, and constants c_8 and c_9 are the number of synapses made by excitatory and inhibitory interneurons on pyramidal cells of voxels within the same area. Thus, the dynamics of the neuronal activity in a cortical voxel is described by a system of 16 differential equations:

$$\dot{y}_1^{nj}(t) = y_9^{nj}(t)$$

$$\dot{y}_2^{nj}(t) = y_{10}^{nj}(t)$$

$$\dot{y}_3^{nj}(t) = y_{11}^{nj}(t)$$

$$\dot{y}_4^{nj}(t) = y_{12}^{nj}(t)$$

$$\dot{y}_5^{nj}(t) = y_{13}^{nj}(t)$$

$$\dot{y}_6^{nj}(t) = y_{14}^{nj}(t)$$

$$\dot{y}_7^{nj}(t) = y_{15}^{nj}(t)$$

$$\dot{y}_8^{nj}(t) = y_{16}^{nj}(t)$$

$$\dot{y}_9^{nj}(t) = Aa \left\{ c_5 S(y_1^{nj}(t) - y_2^{nj}(t)) + c_2 S(y_3^{nj}(t)) + K^{th,n} c_3^t S(x_4(t)) \right\}$$

$$+ Aa \left\{ \sum_{\substack{m=1 \\ m \neq j}}^{M_n} \left(k_{e1}^{mj} c_7 S(y_6^{mn}(t)) + k_{e2}^{mj} c_8 S(y_7^{mn}(t)) \right) \right\}$$

$$\begin{aligned}
& + \sum_{\substack{i=1 \\ i \neq n}}^N K^{i,n} \sum_{m=1}^{M_i} c_6 S(y_5^{im}(t)) \Bigg\} - 2ay_9^{nj}(t) - a^2 y_1^{nj}(t) + Aap^{nj}(t) \\
\dot{y}_{10}^{nj}(t) & = Bb \left\{ c_4 S(y_4^{nj}(t)) + \sum_{\substack{m=1 \\ m \neq j}}^{M_n} k_i^{mj} c_9 S(y_8^{mm}(t)) \right\} - 2by_{10}^{nj}(t) - b^2 y_2^{nj}(t) \\
\dot{y}_{11}^{nj}(t) & = Aa \left\{ c_1 S(y_1^{nj}(t) - y_2^{nj}(t)) + K^{th,n} c_4^t S(x_5(t)) \right\} - 2ay_{11}^{nj}(t) - a^2 y_3^{nj}(t) \\
\dot{y}_{12}^{nj}(t) & = Aa \left\{ c_3 S(y_1^{nj}(t) - y_2^{nj}(t)) + K^{th,n} c_5^t S(x_6(t)) \right\} - 2ay_{12}^{nj}(t) - a^2 y_4^{nj}(t) \\
\dot{y}_{13}^{nj}(t) & = Aa_{d1} S(y_1^{nj}(t) - y_2^{nj}(t)) - 2a_{d1} y_{13}^{nj}(t) - a_{d1}^2 y_5^{nj}(t) \\
\dot{y}_{14}^{nj}(t) & = Aa_{d2} S(y_1^{nj}(t) - y_2^{nj}(t)) - 2a_{d2} y_{14}^{nj}(t) - a_{d2}^2 y_6^{nj}(t) \\
\dot{y}_{15}^{nj}(t) & = Aa_{d3} S(y_3^{nj}(t)) - 2a_{d3} y_{15}^{nj}(t) - a_{d3}^2 y_7^{nj}(t) \\
\dot{y}_{16}^{nj}(t) & = Bb_{d4} S(y_4^{nj}(t)) - 2b_{d4} y_{16}^{nj}(t) - b_{d4}^2 y_8^{nj}(t), \tag{4.1}
\end{aligned}$$

where the superscript nj refers to the voxel j in the area n . The system has extrinsic inputs given by connections from other cortical voxels and the thalamus as well as an intrinsic input $p(t)$ that represents baseline stochastic activity within the voxel. The output is taken as $y_1^{nj}(t) - y_2^{nj}(t)$, which from section 2 can be considered proportional to the generated EEG signal. Note that close voxels separated by the boundary of two neighboring regions are considered to be coupled through LRC solely, even if they are close enough for the SRC to be important. This simplification can easily be avoided by adding relevant terms to the equations for \dot{y}_9^{nj} and \dot{y}_{10}^{nj} in equation 4.1. Nevertheless, in the calculations shown here, all anatomical areas were chosen large enough and the activation regions within each area located distant enough such that boundary effects could be neglected. This allowed us to keep equations simple for the sake of a better understanding of the model.

In the case of the thalamus, the main output of the system is mediated by TC cells, which are assumed to send axonal projections to the three populations of neurons in the cortex: pyramidal, spiny stellate, and smooth stellate cells (see Figure 2). On the contrary, only pyramidal cells project back to the thalamus and make synapses on TC neurons. This model is described by the following set of 12 differential equations:

$$\dot{x}_1(t) = x_7(t)$$

$$\dot{x}_2(t) = x_8(t)$$

$$\begin{aligned}
\dot{x}_3(t) &= x_9(t) \\
\dot{x}_4(t) &= x_{10}(t) \\
\dot{x}_5(t) &= x_{11}(t) \\
\dot{x}_6(t) &= x_{12}(t) \\
\dot{x}_7(t) &= A_t a_t \left\{ \sum_{i=1}^N K^{th,i} \sum_{m=1}^{M_t} c_6 S(y_5^{im}(t)) + p_{th}(t) \right\} - 2a_t x_7(t) - a_t^2 x_1(t) \\
\dot{x}_8(t) &= B_t b_t c_{2t} S(c_{1t} x_3(t)) - 2b_t x_8(t) - b_t^2 x_2(t) \\
\dot{x}_9(t) &= A_t a_t S(x_1(t) - x_2(t)) - 2a_t x_9(t) - a_t^2 x_3(t) \\
\dot{x}_{10}(t) &= A_t a_{d1t} S(x_1(t) - x_2(t)) - 2a_{d1t} x_{10}(t) - a_{d1t}^2 x_4(t) \\
\dot{x}_{11}(t) &= A_t a_{d2t} S(x_1(t) - x_2(t)) - 2a_{d2t} x_{11}(t) - a_{d2t}^2 x_5(t) \\
\dot{x}_{12}(t) &= A_t a_{d3t} S(x_1(t) - x_2(t)) - 2a_{d3t} x_{12}(t) - a_{d3t}^2 x_6(t).
\end{aligned} \tag{4.2}$$

The pulse density input $p_{th}(t)$ in this case can be modeled as the sum of a stimulus (visual or auditory stimulation for example) and a basal random activity in the thalamus. $K^{th,i}$ is the CSPs between the thalamus and the cortical area i and is obtained from the anatomical connectivity matrix as described in section 3.2.

At this point, it is worth making some comments about the mathematical formulation of systems 4.1 and 4.2. The two neural mass models correspond to a mathematical object called random differential equation (RDE) (Hasminskii, 1980 i.e., equations of the form $dx(t) = f(x(t), p(t))dt$, where $p(t)$ is an external stochastic process). Indeed, in equations 4.1 and 4.2, the nonautonomous inputs $p^{nj}(t)$ and $p_{th}(t)$ are external stochastic processes. Note that for each fixed realization of $p^{nj}(t)$ and $p_{th}(t)$, the systems 4.1 and 4.2 are in fact nonautonomous ordinary differential equations. This approach differs from the neural mass models proposed in Jansen and Rit (1995), Wendling et al. (2000), and David and Friston (2003), which mainly use stochastic differential equations (SDE) (i.e., equations of the form $dx(t) = f(x(t))dt + g(x(t))dW(t)$, where the differential $dW(t)$ of the Wiener process $W(t)$ is a gaussian white noise).

Notice that the mathematical formulation of SDEs and RDEs is quite different (Gard, 1988). However, both types of equations are related in the particular case $p(t) = W(t)$. That is, the RDE $dx(t) = f(x(t), p(t))dt$ can be transformed into an SDE by adding the equation $dp(t) = dW(t)$. Hence, the framework of RDEs allows us to consider not only Wiener process but also other types of modeling for the noise $p(t)$. Besides, numerical calculations can be significantly simplified by

avoiding elements of stochastic integration theory usually required in SDEs.

Finally, the existence and uniqueness of the solution of systems 4.1 and 4.2 follow from classical arguments. That is, given a realization of the stochastic processes $p^{nj}(t)$ and $p_{th}(t)$, it is easily seen that the right-hand side of systems 4.1 and 4.2 is given by continuously differentiable functions of their respective arguments (for any choice of the corresponding parameters). Besides, function $S(v(t))$ defined in equation 2.3, the only source of nonlinearity presented on both systems, satisfies a Lipchitz condition (it has first derivative bounded). According to theorem 3.1 in Hasminskii (1980), these two last conditions (continuity and Lipchitz) are enough to guarantee that our model is well posed (i.e., existence and uniqueness of the solution).

5 EEG Observation Model

We now relate the average membrane potential of pyramidal cells of each voxel to the observed EEG on the scalp surface.

The current dipole due to a PSP is approximately (Hämäläinen, Hari, Ilmoniemi, Knuutila, & Lounasmaa, 1993)

$$j = \frac{\pi}{4} d^2 \sigma_{in} \Delta V = \varepsilon \Delta V \quad (5.1)$$

$$\varepsilon = \frac{\pi}{4} d^2 \sigma_{in}, \quad (5.2)$$

where d is the diameter of the dendrite, σ_{in} is the intracellular conductivity, and ΔV is the change of voltage during a PSP (for a single PSP $j \approx 20 fAm$; Hämäläinen et al., 1993). The equivalent current dipole (ECD) due to N PSPs is then

$$J = \sum_{i=1}^N \alpha_i j_i \approx \varepsilon \sum_{i=1}^N \alpha_i \Delta V_i, \quad (5.3)$$

where α_i is +1 for EPSP and -1 for IPSP. As discussed in section 2, we can assume that for one voxel,

$$y_1(t) - y_2(t) = \sum_{i=1}^N \alpha_i \Delta V_i \quad (5.4)$$

and

$$J(t) = \varepsilon (y_1(t) - y_2(t)). \quad (5.5)$$

On the other hand, from the forward problem of the EEG, we know that the voltage measured at the scalp surface due to a current density distribution is given by

$$\phi(\vec{r}_s, t) = \int K(\vec{r}_s, \vec{r}_g) \vec{J}(\vec{r}_g, t) d^3 \vec{r}_g. \quad (5.6)$$

where the kernel $K(\vec{r}_s, \vec{r}_g)$ is the electric lead field, which summarizes the electric and geometric properties of the conducting media (brain, skull, and scalp), and $\vec{J}(\vec{r}_g, t)$ is the primary current density (PCD) vector. The indices s and g run over the sensor (electrodes) and generator (voxels) spaces, respectively, and t denotes time. The lead field matrix $K(\vec{r}_s, \vec{r}_g)$ is commonly known and can be calculated by means of the reciprocity theorem (Plonsey, 1963; Rush & Driscoll, 1969). Thus, the EEG generated due to the activation of one voxel at a given array of electrodes distributed over the scalp surface can easily be calculated by multiplication of the lead field by expression 5.5, both evaluated for the given voxel.

6 Numerical Method

As we mentioned in section 4, an RDE is just a nonautonomous ordinary differential equation (ODE) coupled with a stochastic process ($p(t)$ and $p_{th}(t)$ in our model). Thus, in principle, RDEs can be integrated by applying conventional numerical methods for ODEs. However, it is well known that classical methods in ODEs may introduce “ghost” solutions and numerical instabilities when applied to nonlinear equations, which is critical when dealing with high-dimensional problems (as in our case). On the other hand, very few researchers have studied systematically the properties of such methods for the numerical integration of RDEs (Grune & Kloeden, 2001; Carbonell, Jimenez, Biscay, & de la Cruz, 2005). In this letter we choose the local linearization (LL) for RDE (Carbonell et al., 2005) to solve systems 4.1 and 4.2 (see a description of this method in the appendix). The rationale for this choice is the fact that the LL method improves the order of convergence and stability properties of conventional numerical integrators (Carbonell et al., 2005) for RDEs. Moreover, the LL approach has been key for constructing efficient and stable numerical schemes for the integration and estimation of various classes of random dynamical systems (Shoji & Ozaki, 1998; Prakasa-Rao, 1999; Schurz, 2002).

7 Results

In this section, computational simulations are used to demonstrate the capability of the model to reproduce the temporal dynamics and spectral characteristics of the EEG signal as recorded on the scalp surface. A number of model predictions arising from the results obtained are also shown,

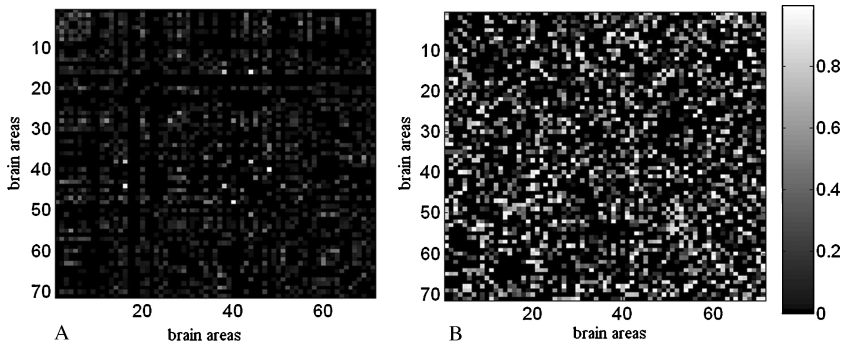


Figure 3: (A) Average anatomical connectivity matrix estimated from diffusion weighted magnetic resonance imaging data of two human subjects. This matrix contains the connection strength between 71 brain areas. These areas were segmented based on the Probabilistic Brain Atlas developed at the Montreal Neurological Institute. The values are normalized between 0 and 1. (B) Random matrix calculated with the same degree of sparseness as that of the anatomical connectivity matrix in A.

and can be further tested experimentally. Additionally, the sensitivity of the results to changes in model parameters is studied.

7.1 Description of the Simulation Method. In the simulations, 71 brain areas were defined based on the Probabilistic MRI Atlas (PMA) produced by the Montreal Neurological Institute (Evans et al., 1993, 1994; Collins, Neelin, Peters, & Evans, 1994; Mazziotta, Toga, Evans, Fox, & Lancaster, 1995). Anatomical connectivity matrices between these areas, corresponding to two human subjects, were then calculated and averaged out. The elements of the resultant average matrix were then used as CSP for between-areas interactions. As shown in Figure 3, the sparseness of this anatomical connectivity matrix allows for a significant reduction in the number of CSPs and thus reduces the computational cost of solving the large RDE system that describes the model presented here.

Initial conditions were set to zero in all simulations, and an integration step size of 5 ms was used. The first 100 points of the simulated signals were discarded in order to avoid transient behavior, and the input $p(t)$ was a gaussian process with mean and standard deviation of 10,000 and 1000 pulses per second, respectively. As for the rest of the model parameter values, they were chosen to vary across space, with values taken from a uniform distribution in the interval between 5% below and above the standard values reported in Table 1. This choice was motivated by the inhomogeneities found in cortical tissue. The motor cortex, for example, has a relatively sparse population of neurons, while sensory cortices tend

Table 1: Values of Model Parameters and Physiological Interpretation.

Parameters with the Same Value in All Simulations		
Parameter	Physiological Interpretation	Value
A, B	Average synaptic gain for cortical voxels	$A = 3.25 \text{ mV}, B = 22 \text{ mV}$
e_0, v_0, r	Parameters of the nonlinear sigmoid function	$e_0 = 5 \text{ s}^{-1}, v_0 = 6 \text{ mV}$ $r = 0.56 \text{ mV}^{-1}$
$\sigma_{e1}, \sigma_{e2}, \sigma_i$	Parameters of the connectivity functions.	$\sigma_{e1} = 10, \sigma_{e2} = 10, \sigma_i = 2$
c_6, c_7, c_8, c_9	Average number of synaptic contacts between the neuronal populations of different cortical voxels	$c_6 = 200, c_7 = 100$ $c_8 = 100, c_9 = 100$
Parameters with Different Values for Each Simulation		
Parameter	Physiological Interpretation	
a, b	Average synaptic time constants for excitatory and inhibitory populations	
$a_{d1}, a_{d2}, a_{d3}, b_{d4}$	Average time delay on efferent connection from a population for cortical voxels	
$c_1, c_2 = 0.8c_1$	Average number of synaptic contacts between the neuronal populations within a cortical voxel	
$c_3 = c_4 = 0.25c_1$		
c_5		
A_t, B_t	Synaptic gain for the thalamus	
c_{1t}, c_{2t}, c_{3t}	Number of synaptic contacts made by the neuronal populations of the thalamus	
c_{4t}, c_{5t}		
a_t, b_t	Average synaptic time constants for TC and RE populations	
Rhythm	Actual Values Used in Each Case	
Delta rhythm	$a = 20 \text{ s}^{-1}, b = 20 \text{ s}^{-1}, a_{d1} = 15 \text{ s}^{-1}, a_{d2} = 20 \text{ s}^{-1}, a_{d3} = 20 \text{ s}^{-1}, b_{d4} = 20 \text{ s}^{-1}, c_1 = 50$	
Theta rhythm	$a = 50 \text{ s}^{-1}, b = 40 \text{ s}^{-1}, a_{d1} = 15 \text{ s}^{-1}, a_{d2} = 50 \text{ s}^{-1}, a_{d3} = 50 \text{ s}^{-1}, b_{d4} = 40 \text{ s}^{-1}, c_1 = 50$	
Alpha rhythm	$a = 100 \text{ s}^{-1}, b = 50 \text{ s}^{-1}, a_{d1} = 33 \text{ s}^{-1}, a_{d2} = 100 \text{ s}^{-1}, a_{d3} = 100 \text{ s}^{-1}, b_{d4} = 50 \text{ s}^{-1}, c_1 = 150, A_t = 3.25 \text{ mV}, B_t = 22 \text{ mV}, c_{1t} = 50, c_{2t} = 50, c_{3t} = 80, c_{4t} = 100, c_{5t} = 80, a_t = 100, b_t = 40$	
Beta rhythm	$a = 100 \text{ s}^{-1}, b = 100 \text{ s}^{-1}, a_{d1} = 33 \text{ s}^{-1}, a_{d2} = 100 \text{ s}^{-1}, a_{d3} = 100 \text{ s}^{-1}, b_{d4} = 100 \text{ s}^{-1}, c_1 = 180$	
Gamma rhythm	$a = 100 \text{ s}^{-1}, b = 100 \text{ s}^{-1}, a_{d1} = 33 \text{ s}^{-1}, a_{d2} = 100 \text{ s}^{-1}, a_{d3} = 100 \text{ s}^{-1}, b_{d4} = 100 \text{ s}^{-1}, c_1 = 250$	

to be more densely populated than the average. Furthermore, even within a given cytoarchitectonic region, cortical thickness and neuronal densities vary considerably (Abeles, 1991). However, despite these differences, it is believed that all cortical regions process information locally according to the same principles. Parameter values will also depend on voxel size. Nevertheless, because it is difficult to establish the exact nature of this dependence, the selection of a plausible range of variation of parameter values (see Table 1) was based on previous modeling studies (Lopes da Silva et al., 1974; Zetterberg et al., 1978; Jansen & Rit, 1995; David & Friston, 2003). Parameters used in previous works and parameters introduced for the first time in this study were then tuned so that the model could produce the different rhythms observed in the human EEG.

In all simulations, our generator space consists of a 3D regular grid of points that represent the possible generators of the EEG inside the brain, while the measurement space is defined by the array of sensors where the EEG is recorded. In this work, 41,850 grid points (defining voxels of size 4.25 mm × 4.25 mm × 4.25 mm) and a dense array of 120 electrodes are placed in registration with the PMA. The 3D grid is further clipped by the gray matter, which consists of all 71 brain regions segmented (18,905 grid points remaining). The electrodes' positions were determined by extending and refining the standard 10/20 system (FP1, FP2, F3, F4, C3, C4, P3, P4, O1, O2, F7, F8, T3, T4, T5, T6, Fz, Cz, and Pz). The physical head model constructed in this way allows us to easily compute the electric lead field matrix that relates the PCD inside the brain to the voltage measured at the sensors' locations.

7.2 Generation of Alpha Rhythm. Experimental data from fMRI as well as solutions of the EEG inverse problem show that generators of the different brain rhythms are not localized in the same cortical areas (Goldman, Stern, Engel, & Cohen, 2002; Martínez-Montes, Valdés-Sosa, Miwakeichi, Goldman, & Cohen, 2004). In the case of the alpha rhythm, it has been demonstrated that increased EEG alpha power is correlated with decreased fMRI signal in multiple regions of occipital, superior temporal, inferior frontal, and cingulate cortex and with increased power in the thalamus and insula (Goldman et al., 2002). In this study, these regions were segmented and subdivided into 12 anatomical areas selected from the PMA (see Table 2), which were further subdivided based on their hemispheric location (left or right). An illustrative visualization of some of these regions with the corresponding fiber tracts estimated from DWMRI is shown in Figure 4A.

The 24 defined brain areas together with their corresponding anatomical connectivity values were used in our model to generate alpha activity; the results are shown in Figure 5. The temporal dynamics and the power spectrum of the signal at the electrodes of maximum amplitude (O1 and O2) show reasonable agreement with experimentally observed EEG (see

Table 2: Brain Areas Selected for Each Rhythm Simulation.

Alpha Rhythm	Delta, Beta, Theta, and Gamma Rhythms
Cuneus (left and right)	Medial front-orbital gyrus (left and right)
Lingual gyrus (left and right)	Middle frontal gyrus (left and right)
Lateral occipitotemporal gyrus (left and right)	Precentral gyrus (left and right)
Insula (left and right)	Lateral front-orbital gyrus (left and right)
Inferior occipital gyrus (left and right)	Medial frontal gyrus (left and right)
Superior occipital gyrus (left and right)	Superior frontal gyrus (left and right)
Medial occipitotemporal gyrus (left and right)	Inferior frontal gyrus (left and right)
Occipital pole (left and right)	
Cingulate region (left and right)	
Inferior frontal gyrus (left and right)	
Superior temporal gyrus (left and right)	
Thalamus (left and right)	

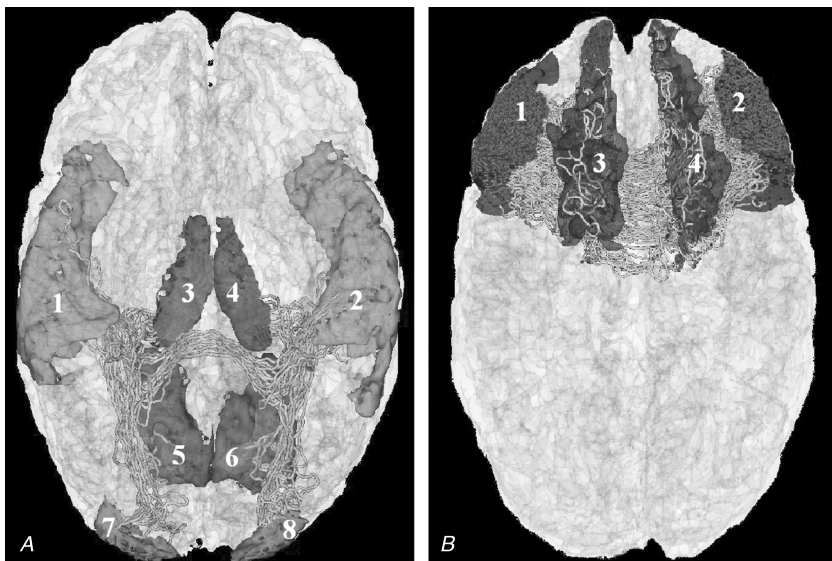


Figure 4: Visualization of the fiber tracts connecting the brain regions used in the simulations as calculated from DWMRI. (A) Alpha rhythm: left and right superior temporal gyri (1, 2); left and right thalamus (3, 4); left and right medial occipitotemporal gyri (5, 6); left and right occipital poles (7, 8). (B) Beta, gamma, delta, and theta rhythms: left and right superior frontal gyri (1, 2); left and right inferior frontal gyri (3, 4).

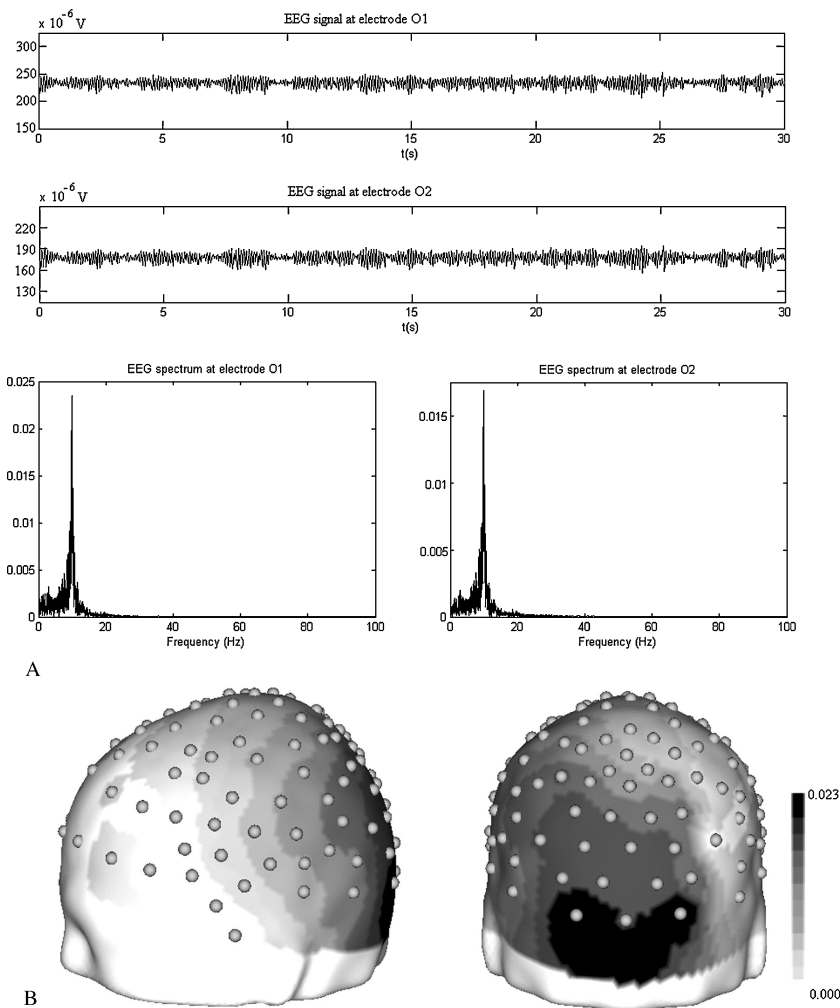


Figure 5: Simulation of alpha rhythm (8–12 Hz). (A) Temporal dynamics and spectrum of the signal at electrodes O1 and O2. (B) Topographic distribution of the alpha power on the scalp surface. The spatial distribution of the 120 electrodes' system used in the simulation is also shown.

Figure 5A). The amplitude of the signal varies between 30 and 50 μ V for both electrodes, and the maximum of the spectrum was at 9.98 Hz for electrode O1 and 9.90 Hz for electrode O2. These values are in the range of actual recordings. Other qualitative properties, like the waxing and waning characteristic of actual alpha rhythm, as well as interhemispheric symmetry, are also observed. Regarding the topographic distribution of the activity,

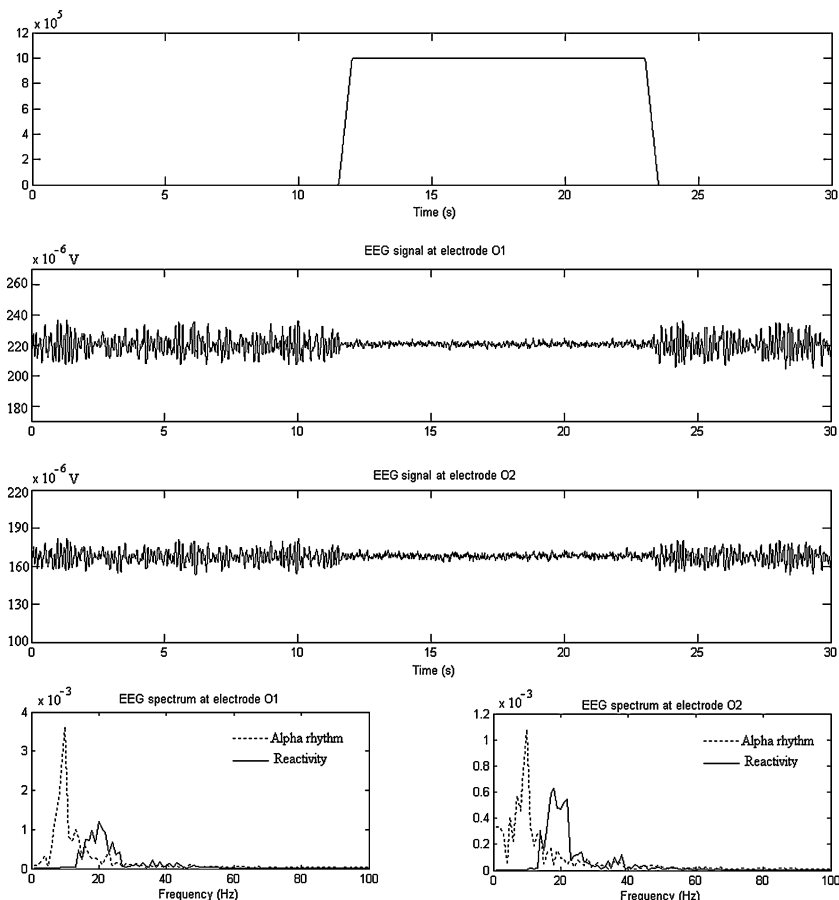


Figure 6: Reactivity test simulation. A trapezoidal input of 12 seconds duration and amplitude of 10^6 pulses per second is used to simulate visual input at the thalamic level. The response of the system results in a significant reduction in the amplitude of both the signal and the peak of the alpha power and a shift of the power spectrum toward higher frequencies.

Figure 5B shows that the simulated EEG is maximal over the occipital regions and diminishes in amplitude toward frontal areas, which has also been described for alpha rhythm.

The influence of an external input (stimulus) on the simulated alpha activity was also studied, and results are depicted in Figure 6. Actual alpha rhythm is known to be temporarily blocked by an influx of light (eye opening). This is known as reactivity. The degree of reactivity varies; the alpha rhythm may be blocked, suppressed, or attenuated with voltage

reduction (Niedermeyer & Lopes da Silva, 1987). In the simulations shown in Figure 6, a trapezoidal input representing visual stimulation of 12 seconds duration and amplitude of 10^6 pulses per second was given to the thalamus. As shown in the figure, the effect of this input was to attenuate the EEG signal and shift the whole EEG spectrum toward higher frequencies with a reduction in the amplitude of the power, which is also observed in actual reactivity tests.

7.3 Generation of Delta, Theta, Beta, and Gamma Rhythms. For the simulation of delta, theta, beta, and gamma rhythms, 7 brain regions (medial-front orbital gyrus, middle frontal gyrus, precentral gyrus, lateral-front orbital gyrus, medial frontal gyrus, superior frontal gyrus, and inferior frontal gyrus) were selected and subdivided based on their hemispheric location (left or right), for a total of 14 brain areas. Some of these areas, with the corresponding fiber tracts connecting them, are shown in Figure 4B.

In these studies, 30 seconds of EEG data were simulated for each rhythm. Figures 7, 8, 9, and 10 show the temporal dynamics and the spectrum of the signal obtained at electrodes Fp1 and Fp2 for the delta, theta, beta, and gamma rhythms simulations, respectively. Amplitudes and spectral frequency bands obtained are within the range of experimentally observed EEG. Note the characteristic interhemispheric asymmetry in the frequency of the peak for the beta rhythm (see Figure 9). That is, the maximum of the spectrum is located at 18.46 Hz for electrode Fp1 and at 16.76 Hz for electrode Fp2. The rest of the simulated rhythms do not show a significant interhemispheric frequency asymmetry. Finally note that the power spectrum on the scalp surface was maximum at frontal areas in all cases and reaches minimum amplitudes at occipital electrodes.

7.4 Influence of the Model Parameters on the Generation of the EEG Rhythms. Parameter values in Table 1 show that by increasing c_1 (and thus c_2 , c_3 , and c_4), while keeping the other parameters constant, the EEG spectrum shifts toward higher frequencies, going from beta to gamma frequency bands. On the other hand, keeping c_1 constant, we can switch from delta to theta rhythm by increasing parameters associated with membrane time constants and dendritic tree time delays. However, as there are 32 parameters in the model (excluding the connectivity matrix values), it is difficult to study the influence of each of them on the output of the model. That is, parameter values presented in Table 1 are not the only ones capable of producing EEG rhythms. Additionally, neural mass models can produce the same EEG rhythm with different sets of parameter values, as shown by David and Friston (2003), which varied excitatory and inhibitory time constants and obtained regions of the parameters' phase-space within which the same rhythm was obtained. In this section, we perform similar analyses for parameters a and b .

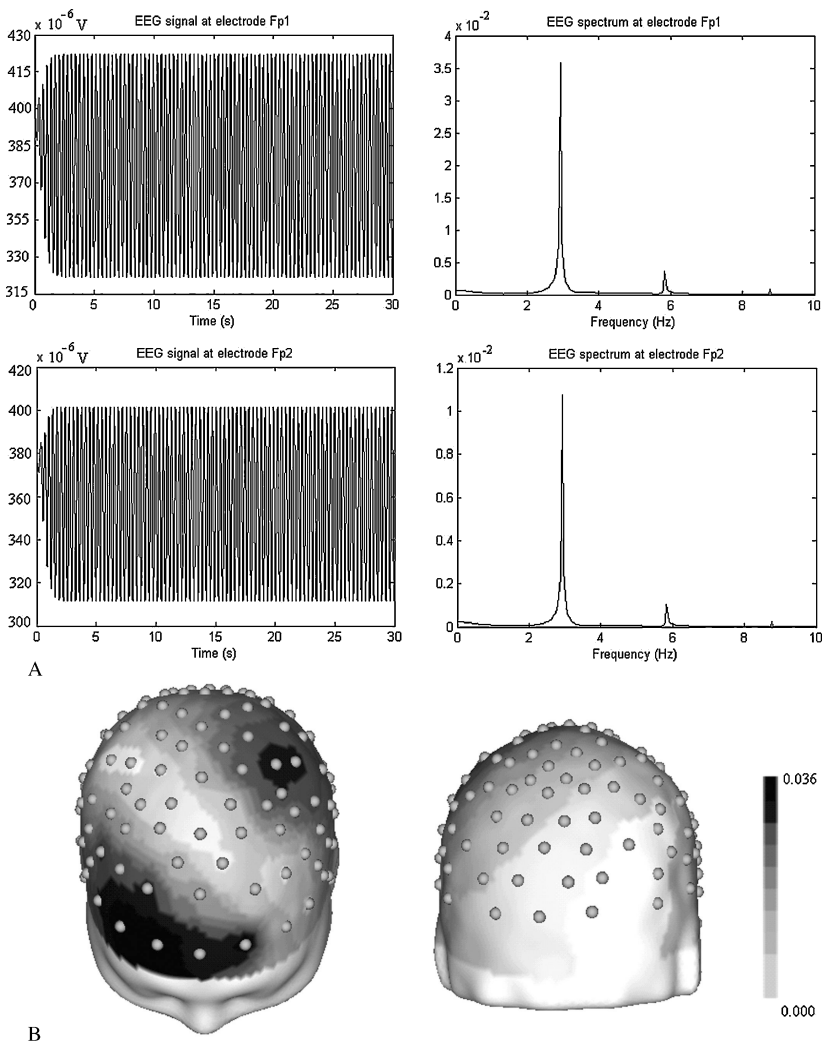


Figure 7: Simulation of delta rhythm (1–4 Hz). (A) Temporal dynamics and power spectrum of the signal at electrodes Fp1 and Fp2. (B) Topographic distribution of the delta power on the scalp surface. The spatial distribution of the 120 electrodes' system used in the simulation is also shown.

In the first set of simulations the areas involved in the alpha rhythm simulation study were selected, and then parameters a, b were varied from 10 s^{-1} to 500 s^{-1} , with a step size of 10 s^{-1} , while the rest of the parameters were kept constant with the values in Table 1 that correspond to alpha rhythm. For each case, the resulting dynamics was assigned to an EEG

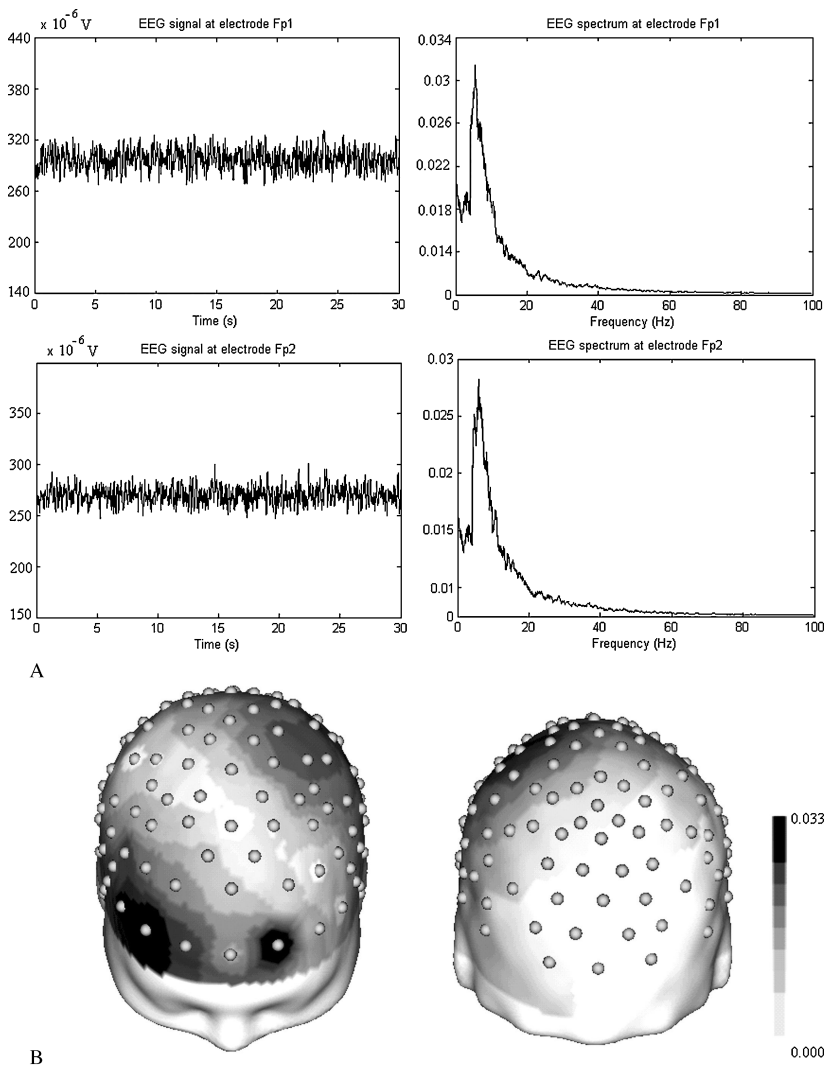


Figure 8: Simulation of theta rhythm (4–8 Hz). (A) Temporal dynamics and power spectrum of the signal at electrodes Fp1 and Fp2. (B) Topographic distribution of the theta power on the scalp surface. The spatial distribution of the 120 electrodes' system used in the simulation is also shown.

band. A phase diagram is shown in Figure 11A. Two phases are obtained depending on parameter values: one corresponding to alpha rhythms and the other corresponding to noise.

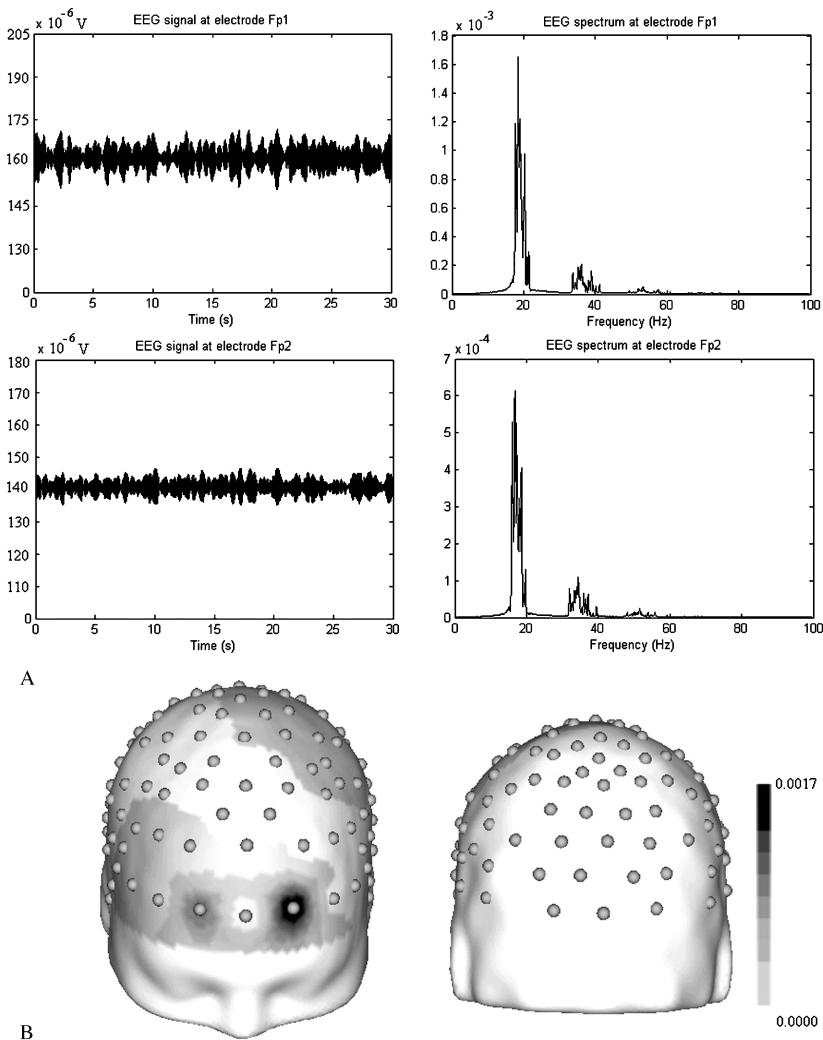


Figure 9: Simulation of beta rhythm (12–30 Hz). (A) Temporal dynamics and power spectrum of the signal at electrodes Fp1 and Fp2. (B) Topographic distribution of the theta power on the scalp surface. The spatial distribution of the 120 electrodes' system used in the simulation is also shown.

In the second study, parameters a , b were also varied from 10 s^{-1} to 500 s^{-1} with a step size of 10 s^{-1} , but now the brain areas selected were the ones involved in the generation of delta, theta, beta, and gamma rhythms. As in the previous case, the other parameters were kept constant with the values shown in Table 1 for beta rhythm. The corresponding phase diagram

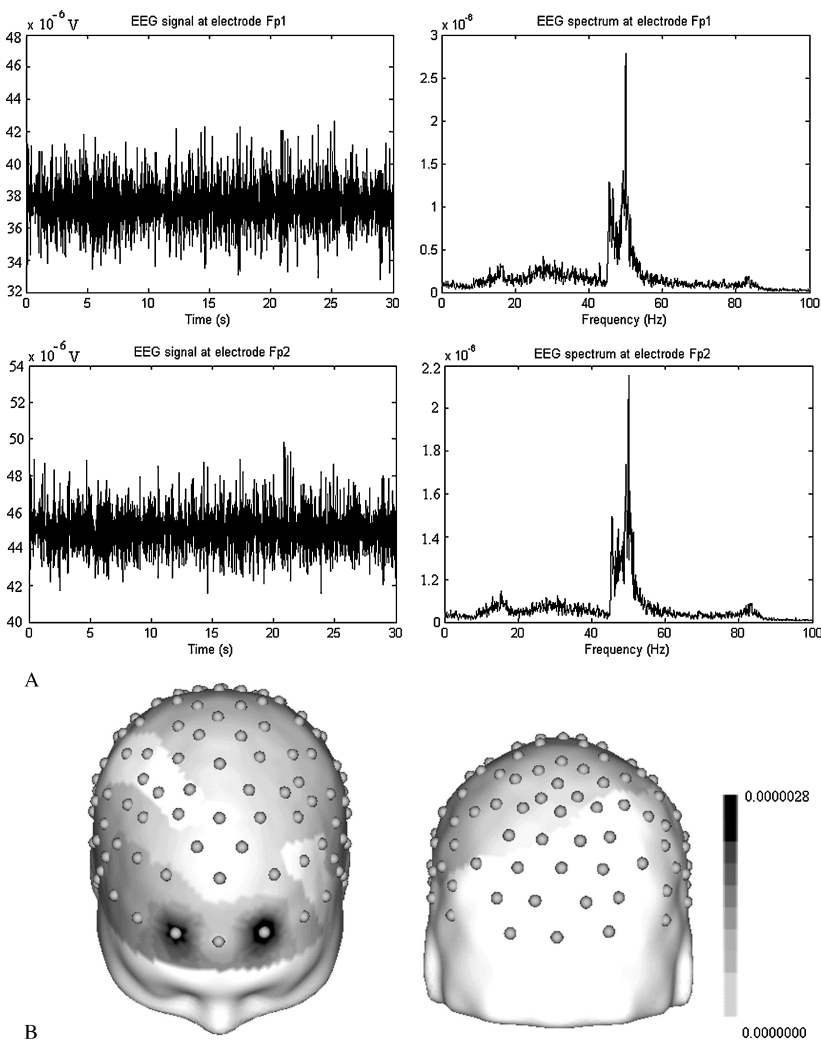


Figure 10: Simulation of gamma rhythm (30–70 Hz). (A) Temporal dynamics and power spectrum of the signal at electrodes Fp1 and Fp2. (B) Topographic distribution of the gamma power on the scalp surface. The spatial distribution of the 120 electrodes' system used in the simulation is also shown.

is shown in Figure 11B. As can be seen, five different phases are obtained corresponding to delta, theta, beta, and gamma rhythms, as well as noise. However, alpha rhythm (the small spots in white between theta and beta areas in Figure 11B) was also obtained for three pairs of values (b, a): (340,180), (340,190), (120,280).

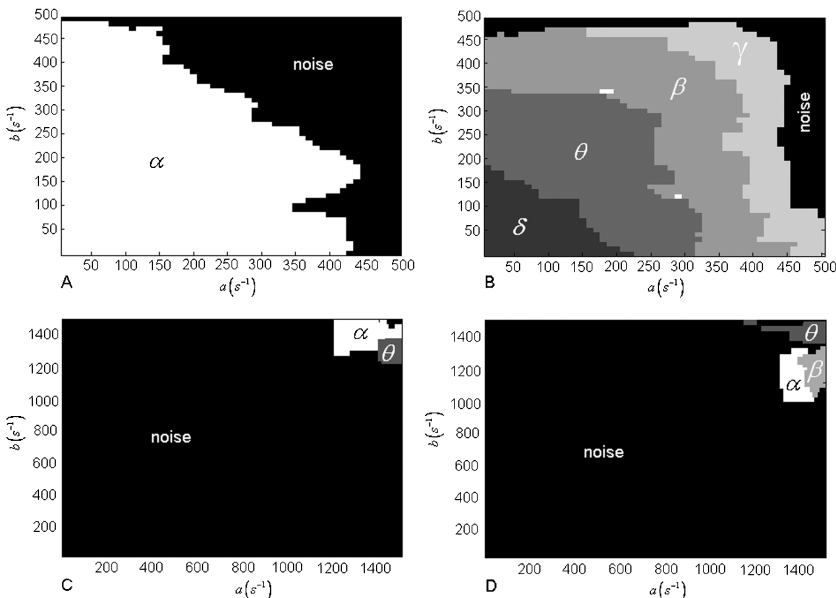


Figure 11: Phase-space diagram of the average synaptic time constants for excitatory (a) and inhibitory (b) populations. (A) The chosen regions were the ones used previously in the alpha rhythm simulation. The phase space splits into two regions that separate noise from alpha rhythm. (B) The selected areas were the ones used in delta, theta, beta, and gamma rhythm simulations. The phase space splits into different regions—one for each rhythm and noise. Nevertheless, for three pairs of values (b, a), alpha rhythm was also obtained (white points between theta and beta areas). (C) The same areas as in A were selected but with values extracted from the random matrix of Figure 3B. (D) The same areas as in B but with values extracted from the random matrix. In C and D, for very large physiologically unrealistic values of (b, a), several rhythms appear.

Thus, by changing a or b , or both, the system undergoes phase transitions that allow the same model to generate the different EEG rhythm. Note also that, as expected, in both sets of simulations, noise is obtained for high values of a or b , or both, which corresponds to processes decaying very rapidly and thus occurring at very high (nonphysiological) frequencies.

One of the main goals of this article is the validation of the use of anatomical connectivity information obtained from DWMRI to model the LRC strength between multiple coupled neural mass models representing cortical areas and the capability of this modeled system to generate different EEG rhythms. So far, we have proven that our model is capable of generating alpha, delta, theta, beta, and gamma rhythm in a wide range of parameter values. Nevertheless, an important question remains: How important is the

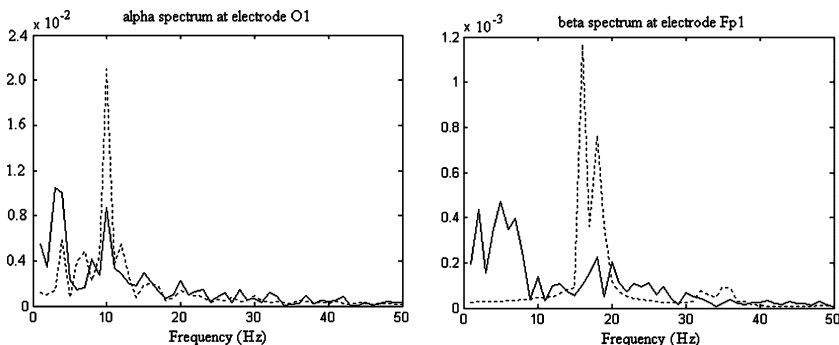


Figure 12: Effect of the reduction of connectivity parameters on alpha and beta rhythms. CSPs between areas were diminished by 50%, and parameter c_1 was also diminished to $c_1 = 50$. The dotted line is the spectrum when using the standard values, and the solid line represents the reduced parameters.

use of the actual connectivity matrix values? In other words, wouldn't be possible to generate EEG rhythms with a completely different connectivity matrix?

To elucidate this matter, the two sets of simulations previously described were replicated, but in this case, the random connectivity matrix shown in Figure 3B was used instead for the coupling between the brain areas involved in the simulations. This random matrix was generated with the same degree of sparseness as the actual connectivity matrix. Results are shown in Figures 11C and 11D. As can be seen, no rhythm emerged for the range of values (b, a) from 10 s^{-1} to 500 s^{-1} in these cases. Only for extremely high and nonphysiological values (corresponding to average population time constants of less than 1 ms) are some rhythms obtained.

An interesting case is to analyze the impact of decreased connection strengths (see section 8). For this, the values of the anatomical connectivity matrix were decreased 50% and parameter c_1 was reduced to $c_1 = 50$ for the cases of the alpha and beta rhythms generation models. The results are shown in Figure 12. For both alpha and beta, the peak amplitude of the power spectrum reduces for its corresponding frequency bands, while the delta and theta bands were accentuated.

8 Discussion

In this work, previous neural mass models (Lopes da Silva et al., 1974; Zetterberg et al., 1978; Jansen & Rit, 1995) were generalized and combined to account for intravoxel interactions, as well as short-range and long-range connections representing interactions between cortical voxels within the same area and with voxels of other cortical areas, respectively. The thalamus

was also described by a neural mass model and coupled to the cortical areas. Anatomical information from DWMRI was introduced to constrain coupling strength parameters between different brain regions. This allowed us to couple multiple brain areas with real anatomical connectivity values and study the rhythms emerging from these interactions across different spatial scales. Knowing the average depolarization of pyramidal cells in each voxel and the lead field matrix that characterizes the spatial distribution of the electromagnetic field in the head, we obtained the voltage signals recorded at the location of given electrodes on the scalp surface.

For validating the model, several simulations were carried out. The parameters that were tuned in each simulation were the time delays of efferent connections and connectivity constants between the different populations within a voxel. The choice of parameter was given by its importance in the generation of different rhythms, as demonstrated by previous work in this field (Jansen & Rit, 1995; David & Friston, 2003). The temporal dynamics and the spectrum of human EEG rhythms were reproduced by the proposed model. EEG rhythms were also obtained at the right spatial locations. In the case of alpha rhythm, the activity was maximal at occipital electrodes and diminished toward the frontal electrodes. Delta, theta, beta, and gamma rhythms were maximal at frontal electrodes. The amplitudes of the rhythms were also within the range observed in actual EEG recordings. Interhemispheric symmetry was found in the case of alpha rhythm, since the difference between the peaks of EEG spectrum at electrodes O1 and O2 was less than 0.1 Hz. In contrast beta rhythm showed interhemispheric asymmetry; that is, there was a difference of 1.7 Hz between the peaks of the EEG spectrum at Fp1 and Fp2. For delta, theta, and gamma rhythms, interhemispheric symmetry with respect to the peak frequency of the spectrum was obtained. In clinical practice, no EEG is complete without a reactivity test (Niedermeyer & Lopes da Silva, 1987). For this reason, we made a reactivity test simulation, finding that the effect of stimulation was to shift the spectrum toward higher frequencies together with a reduction in amplitude, which also agrees with actual EEG recordings in healthy subjects.

Instead of the anatomical connectivity matrix, values from a random matrix were also used to couple brain areas. In this case, some rhythms appear for extremely high values of parameters a and b . However, these values of a and b correspond to an average population time constant of less than 1 ms, which does not make much sense from the physiological point of view. Thus, it can be concluded that in the range of physiologically plausible values, no rhythm was obtained when using a nonrealistic connectivity matrix.

Finally, the model was used to study the effect of a reduction in all connectivity parameters values predicting an increase in delta and theta power (see Figure 12), along with a decrease in alpha and beta peaks. It is

interesting to note that this slowing of oscillatory activity is a prominent functional abnormality that has been reported in EEG and MEG studies of Alzheimer disease (AD) patients (Coben, Danziger, & Berg, 1983; Penttilä, Partanen, Soininen, & Riekkinen, 1985; Schreiter-Gasser, Gasser, & Ziegler, 1993; Berendse, Verbunt, Scheltens, van Dijk, & Jonkman, 2000). On the other hand it is also recognized that AD patients show a progressive cortical disconnection syndrome due to the loss of large pyramidal neurons in cortical layers III and V (Pearson, Esiri, Hiorns, Wilcock, & Powell, 1985; Morrison, Scherr, Lewis, Campbell, & Bloom, 1986). Related to this, it has also been found that the total callosal area is significantly reduced in patients suffering from this pathology (Rose et al., 2000; Hampel et al., 1998). According to our model, the shift of the EEG spectrum toward low frequencies found in AD could be associated with the cortical disconnection syndrome that is reflected in the decreased values of the coupling strength parameters, although the model does not exclude contributions from other mechanisms.

As we know, lumped models are simplifications of actual brain structures, so further improvements could be made by including more realistic models in order to describe a wider range of phenomena. Another limitation of our approach is that DWMRI cannot distinguish between efferent and afferent fibers (this is reflected in the symmetry of the connectivity matrix; see Figure 3A), and connectivity values thus could be overestimated. Moreover, the validity of the connectivity matrix values depends on the assumption that probabilistic paths calculated based on the information obtained from DWMRI reflect the actual connections between brain areas.

While this letter focused on the EEG forward problem, the next logical step is the estimation of the parameters of this model from data. Previous work has accomplished this task. For example, in Valdes et al. (1999), the neural mass model described in Zetterberg et al. (1978) was fitted to actual EEG alpha data. In that work, the LL approach was used to discretize Zetterberg's model, which was then reformulated in a state-space formalism that could be integrated by using a nonlinear Kalman filter scheme. A maximum likelihood procedure was then employed to estimate the model parameters for several EEG data sets. Bayesian inference, dynamic causal modeling (Friston, Harrison, & Penny, 2003; David, Harrison, Kilner, Penny, & Friston, 2004), and genetic algorithms (Jansen, Balaji Kavaipatti, & Markusson, 2001) have also been used for estimating the parameters of neural mass models of the type presented here. A more ambitious goal is the integration of EEG with functional imaging techniques such as functional magnetic resonance imaging and positron emission tomography. The use of this model as a framework in which electrical, hemodynamic, and metabolic activities can be coupled is currently under study and will be the subject of a future publication.

Appendix: Local Linearization Method for RDE

Assume that a k -dimensional random process $p(t)$, $t \in [t_0, T]$ and a non-linear function f are given, and define the d -dimensional RDE:

$$dy(t) = f(y(t), p(t))dt$$

$$y(t_0) = y_0.$$

Then, given a step size h , the local linearization scheme that solves numerically the equation above at the time instants $t_n = t_0 + nh$, $n = 0, 1, \dots$, is given by

$$y_{n+1} = y_n + L e^{C_n h} R,$$

where $L = [I_d, 0_{d \times 2}]$, $R = [0_{1 \times (d+1)}, 1]^T$, and the $(d+2) \times (d+2)$ matrix C_n is defined by blocks as

$$C_n = \begin{pmatrix} \dot{f}_y(t)(y_n, p(t_n)) & \dot{f}_p(t)(y_n, p(t_n)) \frac{p(t_{n+1}) - p(t_n)}{h} & f(y_n, p(t_n)) \\ 0 & 0 & 1 \\ 0 & 0 & 0 \end{pmatrix}$$

Here, $\dot{f}_y(t)$ and $\dot{f}_p(t)$ denote the derivatives of f with respect to the variables y and p , respectively.

Due to the high dimensionality of our problem, the main task in the implementation of the LL scheme is the computation of the matrix exponential $e^{C_n h}$. The use of the Krylov subspace methods (Sidje, 1998) is strongly recommended for that purpose. Indeed, that method can be used to compute the vector $v = e^{C_n h} R$, and then the operation Lv reduces to take the first d elements of v .

Acknowledgments

We thank Trinidad Virues, Elena Cuspineda, and Thomas Wennekers for helpful comments.

References

- Abeles, M. (1991). *Corticonics: Neural circuits of the cerebral cortex*. Cambridge: Cambridge University Press.
- Behrens, T., Johansen-Berg, H., Woolrich, M. W., Smith, S. M., Wheeler-Kingshott, C., Boulby, P. A., Barker, G. J., Sillery, E. L., Sheehan, K., Ciccarelli, O., Thompson, A. J., Brady, J. M., & Matthews, P. M. (2003). Non-invasive mapping of connections between human thalamus and cortex using diffusion imaging. *Nature Neuroscience*, 6, 750–757.

- Berendse, H. W., Verbunt, J. P., Scheltens, P., van Dijk, B. W., & Jonkman, E. J. (2000). Magnetoencephalographic analysis of cortical activity in Alzheimer's disease: A pilot study. *Clin. Neurophysiol.*, 111, 604–612.
- Braitenberg V. (1978). Cortical architectonics: General and areal. In M. A. B. Brazier and M. Petche (Eds.), *Architectonics of the cerebral cortex* (pp. 443–465). New York: Raven Press.
- Braitenberg, V., & Schüz, A. (1998). *Cortex: Statistics and geometry of neuronal connectivity*. Berlin: Springer-Verlag.
- Carbone, F., Jimenez, J. C., Biscay, R. J., & de la Cruz, H. (2005). The local linearization method for numerical integration of random differential equations. *BIT Numerical Mathematics*, 45(1), 1–14.
- Coben, L. A., Danziger, W. L., & Berg, L. (1983). Frequency analysis of the resting awake EEG in mild senile dementia of Alzheimer type. *Electroencephalogr. Clin. Neurophysiol.*, 55, 372–380.
- Collins, D. L., Neelin, P., Peters, R. M., & Evans, A. C. (1994). Automatic 3D inter-subject registration of MR volumetric in standardized Talairach space. *J. Comp. Assist. Tomogr.*, 18, 192–205.
- David, O., & Friston, K. J. (2003). A neural mass model for MEG/EEG: Coupling and neuronal dynamics. *NeuroImage*, 20, 1743–1755.
- David, O., Harrison, L., Kilner, J., Penny, W., & Friston, K. J. (2004). Studying effective connectivity with a neural mass model of evoked MEG/EEG responses. In *Proceedings of the 14th International Conference on Biomagnetism BIOMAG 2004* (pp. 136–138). Boston.
- Destexhe, A., & Sejnowski, T. J. (2001). *Thalamocortical assemblies: How ion channels, single neurons, and large-scale networks organize sleep oscillations*. New York: Oxford University Press.
- Douglas, R. J., & Martin, K. A. C. (2004). Neuronal circuits of the neocortex. *Annu. Rev. Neurosci.*, 27, 419–51.
- Evans, A. C., Collins, D. L., Mills, S. R., Brown, E. D., Kelly, R. L & Peters, T. M. (1993). 3D statistical neuroanatomical models from 305 MRI volumes. Proc. In *IEEE Nuclear Science Symposium and Medical Imaging Conference* (pp. 1813–1817). London: MTP Press.
- Evans, A. C., Collins, D. L., Neelin, P., MacDonald, D., Kamber, M., & Marrett, T. S., 1994. Three-dimensional correlative imaging: Applications in human brain mapping. In: Thatcher, R., Hallet, M., Zeffiro, T., John, E. R., & Huerta, M. (Eds.), *Functional Neuroimaging: Technical Foundations*. Academic Press, New York, pp. 145–161.
- Friston, K. J., Harrison, L., & Penny, W. (2003). Dynamic causal modelling. *NeuroImage*, 19, 1273–1302.
- Gard, T. C. (1988). *Introduction to stochastic differential equations*. New York: Marcel Dekker.
- Gilbert, C. D., & Wiesel, T. N. (1979). Morphology and intracortical projections of functionally characterised neurones in the cat visual cortex. *Nature*, 280, 120–125.
- Gilbert, C. D., & Wiesel, T. N. (1983). Functional organization of the visual cortex. *Prog. Brain Res.*, 58, 209–218.
- Goldman, R. I., Stern, J. M., Engel, J., & Cohen, M. S. (2002). Simultaneous EEG and fMRI of the alpha rhythm. *NeuroReport*, 13(18), 2487–2492.

- Grune, L., & Kloeden, P. E. (2001). Pathwise approximation of random ordinary differential equation. *BIT*, 41, 711–721.
- Hagmann, P., Thiran, J. P., Jonasson, L., Vandergheynst, P., Clarke, S., Maeder, P., & Meuli, R. (2003). DTI mapping of human brain connectivity: Statistical fibre tracking and virtual dissection. *NeuroImage*, 19, 545–554.
- Hämäläinen, M., Hari, R., Ilmoniemi, R. J., Knuutila, J., & Lounasmaa, O. V. (1993). Magnetoencephalography—theory, instrumentation and applications to non-invasive studies of the working human brain. *Rev. Modern Phys.*, 65, 413–497.
- Hampel, H., Teipel, S. J., Alexander, G. E., Horwitz, B., Teichberg, D., Schapiro, M. B., & Rapoport, S. I. (1998). Corpus callosum atrophy is a possible indicator of region- and cell type-specific neuronal degeneration in Alzheimer disease: A magnetic resonance imaging analysis. *Arch. Neurol.*, 55, 193–198.
- Hasminskii, R. Z. (1980). *Stochastic stability of differential equations*. Alphen aan den Rijn, The Netherlands: Sijhoff Noordhoff.
- Iturria-Medina, Y., Canales-Rodríguez, E., Melié-García, L., & Valdés-Hernández, P. (2005). Bayesian formulation for fiber tracking. Presented at the 11th Annual Meeting of the Organization for Human Brain Mapping, Toronto, Ontario, Canada.
- Iturria-Medina, Y., Valdés-Hernández, P., & Canales-Rodríguez, E. (2005). Measures of anatomical connectivity obtained from neuro diffusion images. Presented at the 11th Annual Meeting of the Organization for Human Brain Mapping, Toronto, Ontario, Canada.
- Jansen, B. H., Balaji Kavaipatti, A., & Markusson, O. (2001). Evoked potential enhancement using a neurophysiologically-based model. *Methods of Information in Medicine*, 40, 338–345.
- Jansen, B. H., & Rit, V. G. (1995). Electroencephalogram and visual evoked potential generation in a mathematical model of coupled cortical columns. *Biol. Cybern.*, 73, 357–366.
- Jansen, B. H., Zouridakis, G., & Brandt, M. E. (1993). A neurophysiologically-based model of flash visual evoked potentials. *Biol. Cybern.*, 68, 275–283.
- Jirsa, V. K., & Haken, H. (1996). Field theory of electromagnetic brain activity. *Phys. Rev. Lett.*, 77(5), 960–963.
- Jirsa, V. K., & Haken, H. (1997). A derivation of a macroscopic field theory of the brain from the quasi-microscopic neural dynamics. *Physica D*, 99, 503–526.
- Koch, M. A., Norris, D. G., & Hund-Georgiadis, M. (2002). An investigation of functional and anatomical connectivity using magnetic resonance imaging. *NeuroImage*, 16, 241–250.
- Lopes da Silva, F. H., Hoeks, A., Smits, H., & Zetterberg, L. H. (1974). Model of brain rhythmic activity: The alpha-rhythm of the thalamus. *Kybernetik*, 15, 27–37.
- Martin, K. A. C., & Whitteridge, D. (1984). Form, function and intracortical projections of spiny neurones in the striate visual cortex of the cat. *J. Physiol.*, 353, 463–504.
- Martínez-Montes, E., Valdés-Sosa, P. A., Miwakeichi, F., Goldman, R. I., & Cohen, M. S. (2004). Concurrent EEG/fMRI analysis by multiway partial least squares. *NeuroImage*, 22, 1023–1034.
- Mazziotta, J. C., Toga, A., Evans, A. C., Fox, P., & Lancaster, J. (1995). A probabilistic atlas of the human brain: Theory and rationale for its development. *Neuroimage*, 2, 89–101.

- McGuire, B. A., Gilbert, C., Rivlin, P. K., & Wiesel, T. N. (1991). Targets of horizontal connections in macaque primary visual cortex. *J. Comp. Neurol.*, 305, 370–392.
- Morrison, J. H., Scherr, S., Lewis, D. A., Campbell, M. J., & Bloom, F. E. (1986). The laminar and regional distribution of neocortical somatostatin and neuritic plaques: Implications for Alzheimer's disease as a global neocortical disconnection syndrome. In A. B. Scheibel, A. F. Weschler (Eds.), *The biological substrates of Alzheimer's disease* (pp. 115–131). New York: Academic Press.
- Mountcastle V. B. (1978). An organizing principle for cerebral function. In G. M. Edelman, V. B. Mountcastle (Eds.), *The mindful brain* (pp. 7–50). Cambridge, MA: MIT Press.
- Mountcastle, V. B. (1997). The columnar organization of the neocortex. *Brain*, 120, 701–722.
- Niedermeyer, E. & Lopes da Silva, F. (1987). *Electroencephalography: Basic principles-clinical applications and related fields* (2nd ed.). Baltimore: Urban & Schwarzenberg.
- Nunez, P. L. (1981). *Electric fields of the brain*. New York: Oxford University Press.
- Parker, G. J., Wheeler-Kingshott, C. A., & Barker, G. J. (2002). Estimating distributed anatomical connectivity using fast marching methods and diffusion tensor imaging. *IEEE Transactions on Medical Imaging*, 21(5), 505–512.
- Pearson, R. C. A., Esiri, M. M., Hiorns, R. W., Wilcock, G. K., & Powell, T. P. S. (1985). Anatomical correlates of the distribution of the pathological changes in the neocortex in Alzheimer's disease. *Proc. Natl. Acad. Sci. USA*, 82, 4531–4534.
- Penttilä, M., Partanen, J. V., Soininen, H., & Riekkinen, P. J. (1985). Quantitative analysis of occipital EEG in different stages of Alzheimer's disease. *Electroencephalogr. Clin. Neurophysiol.*, 60, 1–6.
- Plonsey, R. (1963). Reciprocity applied to volume conductors and the ECG. *IEEE Trans. BioMedical Electronics*, 10, 9–12.
- Prakasa-Rao, B. L. S. (1999). *Statistical inference for diffusion type processes*. New York: Oxford University Press.
- Rinzel, J., Terman, D., Wang, X.-J., & Ermentrout, B. (1998). Propagating activity patterns in large-scale inhibitory neuronal networks. *Science*, 279, 1351–1355.
- Rose, S. E., Chen, F., Chalk, J. B., Zelaya, F. O., Strugnell, W. E., Benson, M., Semple, J., & Doddrell, D. M. (2000). Loss of connectivity in Alzheimer's disease: An evaluation of white matter tract integrity with colour coded MR diffusion tensor imaging. *J. Neurol. Neurosurg. Psychiatry*, 69, 528–530.
- Rush, S., & Driscoll, D. A. (1969). EEG electrode sensitivity—an application of reciprocity. *IEEE Trans on Biomed. Eng.*, 16(1), 15–22.
- Schreiter-Gasser, U., Gasser, T., & Ziegler, P. (1993). Quantitative EEG analysis in early onset Alzheimer's disease: A controlled study. *Electroencephalogr. Clin. Neurophysiol.*, 86, 15–22.
- Schurz H. (2002). Numerical analysis of stochastic differential equations without tears. In D. Kannan & V. Lakshmikantham (Eds.), *Handbook of stochastic analysis applications* (pp. 237–358). New York: Marcell Dekker.
- Shoji, I., & Ozaki, T. (1998). Estimation for nonlinear stochastic differential equations by a local linearization method. *Stochast. Anal. Appl.*, 16, 733–752.
- Sidje, R. B. (1998). EXPOKIT: Software package for computing matrix exponentials. *AMC Trans. Math. Software*, 24, 130–156.

- Tournier, J. D., Calamante, F., Gadian, D. G., & Connelly, A. (2003). Diffusion-weighted magnetic resonance imaging fibre tracking using a front evolution algorithm. *NeuroImage*, *20*, 276–288.
- Traub, R. D., & Miles, R. (1991). *Neuronal networks of the hippocampus*. Cambridge: Cambridge University Press.
- Tuch, D. (2002). Diffusion MRI of complex neural architecture. Unpublished doctoral dissertation, Massachusetts Institute of Technology.
- Valdes, P. A., Jiménez, J. C., Riera, J., Biscay, R., & Ozaki, T. (1999). Nonlinear EEG analysis based on a neural mass model. *Biol. Cybern.*, *81*, 415–424.
- van Rotterdam, A., Lopes da Silva, F. H., van den Ende, J., Viergever, M. A., & Hermans, A. J. (1982). A model of the spatial temporal characteristic of the alpha rhythm. *Bull. Math. Biol.*, *44*, 238–305.
- Wang, X.-J., Golomb, D., & Rinzel, J. (1995). Emergent spindle oscillations and intermittent burst firing in a thalamic model: Specific neuronal parameters. *Proc. Natl. Acad. Sci. USA*, *92*, 5577–5581.
- Wendling, F., Bellanger, J. J., Bartolomei, F., & Chauvel, P. (2000). Relevance of nonlinear lumped-parameter models in the analysis of depth-EEG epileptic signals. *Biol. Cybern.*, *83*, 367–378.
- Wilson, H. R., & Cowan, J. D. (1972). Excitatory and inhibitory interactions in localized populations of model neurons. *Biophys. J.*, *12*, 1–24.
- Zetterberg, L. H., Kristiansson, L., & Mossberg, K. (1978). Performance of a model for a local neuron population. *Biol. Cybern.*, *31*, 15–26.

Received December 20, 2005; accepted June 9, 2006.